Optical properties of the organic-inorganic hybrid perovskite $CH_3NH_3PbI_3$: Theory and experiment

D. O. Demchenko,[1] N. Izyumskaya,[2] M. Feneberg,[3] V. Avrutin,[2] Ü. Özgür,[2] R. Goldhahn,[3] and H. Morkoç[2]

[1]*Department of Physics, Virginia Commonwealth University, Richmond, Virginia 23284, USA*

[2]*Department of Electrical and Computer Engineering, Virginia Commonwealth University, Richmond, Virginia 23284, USA*

[3]*Institut für Experimentelle Physik, Abteilung Materialphysik, Otto-von-Guericke Universität Magdeburg, Universitätsplatz 2, 39106 Magdeburg, Germany*

(Received 17 May 2016; revised manuscript received 22 July 2016; published 17 August 2016)

We perform a theoretical and experimental study of the optical properties of a $CH_3NH_3PbI_3$ perovskite prepared by a vapor-assisted solution process, motivated in part by very high photovoltaic cell efficiencies. Several widespread theoretical approaches are used in an attempt to determine the most appropriate approach which would reproduce the experimental electronic structure and optical properties of the $CH_3NH_3PbI_3$ perovskite. We compare a semilocal approximation to the density functional theory with hybrid functionals and time-dependent hybrid functional calculations, evaluating the effects of exchange tuning and spin-orbit coupling. Using these methods we calculate the electronic structure, optical absorption spectrum, and frequency-dependent dielectric function of the $CH_3NH_3PbI_3$ perovskite. The results are compared to the experimentally obtained dielectric functions acquired from ellipsometry measurements. We demonstrate that inclusion of spin-orbit coupling in theoretical calculations is critical in describing the electronic and optical properties of the $CH_3NH_3PbI_3$ perovskite. Good agreement with experimental data is achieved when the optical spectra are computed using time-dependent hybrid density functional theory with spin-orbit coupling.

DOI: 10.1103/PhysRevB.94.075206

I. INTRODUCTION

Mixed organic-inorganic halide perovskites have recently attracted considerable interest as solar energy harvesters for a new generation of solar cells. Perovskite-based solar cells (PSCs) feature high power conversion efficiencies and potentially low manufacturing costs due to the simplicity of the fabrication procedure [1,2]. The certified energy conversion efficiencies of the PSCs produced using simple wet chemistry routes have progressed from a moderate 3.8% in 2009 to a remarkable 21% in 2015 [3], with prospects for higher efficiencies than those of existing bulk-silicon (26%) and thin-film (21%) single junction solar cells, which dominate today's market. The material commonly used as the light absorber in the PSCs, methylammonium lead triiodide ($CH_3NH_3PbI_3$), adopts the ABX_3 perovskite crystal structure, where A is a cation of an organic compound methylammonium (CH_3NH_3), B is a divalent metal cation (Pb^{2+}), and X is a monovalent halogen anion (I^-). This perovskite compound is inexpensive, solution processable, and exhibits a series of superior electronic and optical properties for solar cell applications: ambipolar charge transport [4], long carrier diffusion lengths [5,6], high optical absorption, and band gaps that can be tailored for efficient solar energy harvesting by varying the chemical composition [7].

In recent years, methylammonium lead triiodide ($CH_3NH_3PbI_3$) perovskites have been explored theoretically using several common approaches, ranging from effective mass to several variations of self-consistent density functional theory (DFT) approaches, as well as quasiparticle methods. Based on DFT calculations, it was shown that the band gap of the $CH_3NH_3PbI_3$ perovskite is strongly affected by a giant spin-orbit coupling (SOC), mainly in the conduction band [8]. The room-temperature optical transitions are between the valence band and a conduction band, which is the spin-orbit split-off band from the triply degenerate conduction band minimum of the cubic lattice in the absence of SOC. It was also suggested that the high performance of solar cells based on these materials is a consequence of their multiband-gap and multivalley nature, making them natural multijunction materials [9]. The inclusion of SOC is thus crucial to obtain the correct electronic and optical structure of the $CH_3NH_3PbI_3$ perovskite.

On the other hand, it was also shown that including SOC in the DFT calculation reduces the band gap by approximately 1 eV, to ∼0.5 eV [10], creating difficulties in comparing theoretical results with experiment. Such a significantly lower value of the calculated band gap is typical for widely used local and semilocal approximations to the DFT. Therefore, it was suggested that purposely omitting the spin-orbit coupling in the calculation, thus increasing the band gap towards the experimental value of ∼1.6 eV, is an effective way to counteract the underestimation of the band gap [11,12]. In the $CH_3NH_3PbI_3$ perovskite this cancellation of two opposing trends is rather effective, and the results obtained by using DFT without SOC showed reasonable agreement with experimental data [13–15].

Alternatively, relativistic quasiparticle GW calculations were performed in order to capture the effects of SOC and accurately determine the band structure [16–18]. These calculations, while being state of the art in electronic structure methods, are very computationally demanding. A reasonable compromise, offering a good trade-off between accuracy and computational cost, is afforded by hybrid functionals. It has been recently shown that hybrid functionals employed along with SOC are able to reproduce some experimental optical quantities of $CH_3NH_3PbI_3$, such as band gap, reduced exciton mass, and exciton binding energy [19]. The authors also showed that tuning the hybrid functional to a high-frequency dielectric constant leads to good agreement with experiment.

The structural properties of the $CH_3NH_3PbI_3$ perovskite present an additional layer of complexity. Standard local

density approximation (LDA) or generalized gradient approximation (GGA) to the DFT is unable to capture the van der Waals interactions. Calculations employing special functionals, which include the nonlocal van der Waals correlations (however, without SOC), suggest that these interactions are critical for appropriate descriptions of the interaction between the organic and the inorganic parts [20]. Such a treatment might be necessary to obtain the realistic crystal structure of $CH_3NH_3PbI_3$. The effects of disorder due to the distortions by rotating organic molecules at room temperature and the asymmetry of the inorganic framework leading to Rashba splitting are also among the currently unsettled issues.

In this paper, we use several widely employed theoretical methods to calculate the electronic structure and optical properties of two common phases of the $CH_3NH_3PbI_3$ perovskite, cubic and tetragonal. We use the GGA approximation to DFT to estimate the effects of SOC on the overall band structure, absorption spectra, and frequency-dependent dielectric function. In order to obtain the correct band structure and optical spectra, we apply the Heyd-Scuseria-Ernzerhof (HSE) hybrid functional [21,22] in both standard and the exact exchange tuned versions, including SOC self-consistently. Finally, the time-dependent HSE approach is used in order to bring the theory to a close agreement with experiment. On the experimental side, we use spectroscopic ellipsometry measurements on the samples grown by a vapor-assisted solution process [23,24]. Spectroscopic ellipsometry allows a parameter-free and very accurate determination of the real and imaginary parts of the dielectric function in the whole spectral region of interest. The ellipsometric data are frequently used for evaluating the results of the combined band-structure and optical property calculations for many materials [25–27].

II. METHODS

A. Calculations

We use several methods of electronic structure calculations to evaluate their suitability to address the experimentally obtained optical and electronic properties of the $CH_3NH_3PbI_3$ perovskite. We use the semilocal GGA parametrization of Perdew-Burke-Ernzerhof (PBE) [28], with the projector augmented wave (PAW) pseudopotentials [29] for atomic relaxations and initial estimations of the electronic structure and SOC effects. The SOC was included in the calculations self-consistently with noncollinear spins according to Ref. [30], and implemented in the VASP code [31,32].

Starting from the experimental lattice structures for cubic and tetragonal phases of $CH_3NH_3PbI_3$, atoms were allowed to relax to minimize the forces to 0.01 eV/Å or less. Plane wave cutoffs of 400 eV were used for lattice relaxation, and 300 eV for subsequent band-structure and optical calculations. Test calculations show negligible differences in band structure and optical spectra with this reduced cutoff energy. For atomic relaxations and calculations of the electronic structure, Γ-point centered k-point grids of $6\times6\times4$ and $6\times6\times6$ were used for the tetragonal and cubic phases, respectively. GGA tests show that $3\times3\times2$ and $4\times4\times4$ k-point grids, used for the tetragonal and cubic phases, result in total energies that are converged to within 2 meV/atom.

In order to obtain an accurate electronic structure, we performed HSE hybrid functional [21,22] calculations. In an exchange-tuned HSE hybrid functional calculation, the semi/local density exchange-correlation part of the density functional is mixed with a Fock-type exchange part in a ratio, which can be adjusted to reproduce the experimental band gap of the material. We start with the standard parametrization of the HSE hybrid functional with a fraction of the exact exchange of 0.25, and a screening parameter of 0.2 $Å^{-1}$. To bring the results to a closer agreement with experiments, we further tune the fraction of exact exchange to recover the experimental band gap, as described below.

The optical properties were computed using two different approaches. First, the imaginary part of the frequency-dependent dielectric function was calculated using the summation of transitions over the conduction band states, which were computed with both standard and exchange-tuned HSE. In turn, the real part of the dielectric function was obtained using the Kramers-Kronig transformation. This method, representing the independent particle approximation, is described in detail in Ref. [33]. Second, to include excitonic effects, time-dependent hybrid functional calculations (TD-HSE) were performed, following Ref. [34], which are based on the exchange-tuned hybrid HSE functional, including SOC self-consistently. In the TD-HSE calculations, the excitonic effects are approximately described by replacing the electron-hole ladder diagrams with the screened exchange. The dielectric function is obtained by solving the Cassida's equation [35]. It has been pointed out that this is essentially equivalent to the Bethe-Salpeter equation, with the screened interaction W replaced with one-quarter of the nonlocal screened exchange term, which is obtained from the standard or exchange-tuned HSE [34]. Both the independent particle approximation method and TD-HSE approach are implemented in VASP [32].

Both approaches to capture optical properties require fairly dense k-point meshes. This is challenging for nonlocal HSE calculations which also self-consistently include SOC. GGA and HSE tests show that for the cubic phase of $CH_3NH_3PbI_3$, both imaginary and real parts of the frequency-dependent dielectric function are sufficiently converged to allow a satisfactory comparison with experiment for an $8\times8\times8$ k-point grid (a $6\times6\times4$ grid for the tetragonal phase). However, a direct calculation on these meshes at the HSE+SO level, where noncollinear spins are included and no symmetry consideration is used, is computationally prohibitive. Therefore, the results were obtained by summing over a number of $4\times4\times4$ k-point grids, shifted with respect to each other to overall reproduce the $8\times8\times8$ grid (sums over a number of $3\times3\times2$ grids were used to reproduce the $6\times6\times4$ grid for the tetragonal phase). All calculations used the Methfessel-Paxton [36] first-order method for partial occupancies with a smearing of 0.2 eV.

B. Experiment

$CH_3NH_3PbI_3$ perovskite samples used for the investigations were prepared by a vapor-assisted solution process [23,24]. At the initial stage, PbI_2 films were fabricated by spin coating of 0.88 M solution PbI_2 (99%, Acros Organics) in N,N-dimethylformamide on sapphire substrates. Prior to

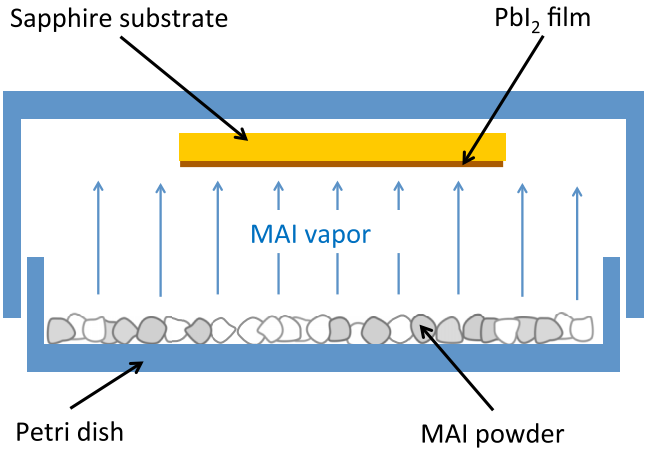

FIG. 1. Schematic describing the synthesis of perovskite layers from a spin-coated inorganic layer by the vapor-assisted solution process.

coating, the substrates were degreased in boiling acetone and boiling methanol. The spin coating was performed in a nitrogen atmosphere at a rate of 1000 rpm for 5 s, followed by 5000 rpm for 40 s. The as-coated films were prebaked on a hotplate at 120 °C for 15 min in nitrogen. Then, the substrates were mounted face down in a petri dish with methylammonium iodide (MAI) powder spread on the underside, as shown in Fig. 1. The MAI powder (>99.9%) was purchased from Ossila Ltd. and used as received. The petri dish was placed in an oven, and maintained at a temperature of 137 °C under nitrogen flow, where the samples were exposed to MAI vapor. After annealing for 3 h, dark-brown $CH_3NH_3PbI_3$ perovskite films were obtained.

The morphology and structural properties of the perovskite layers were examined by optical and atomic-force microscopy (AFM), as well as x-ray diffraction (XRD). The microscopy imaging evidenced the formation of continuous films. From the AFM measurements, the root mean square roughness of the perovskite films was determined to be 26 nm for $20\times20\,\mu$m [2] scans. XRD ω-2θ scans showed reflections at 14°, 23.1°, 28.3°, 31.8°, 34.8°, and 43.2° corresponding to the tetragonal perovskite structure of $CH_3NH_3PbI_3$ [37,38]. The absence of a peak at 12.6° related to PbI_2 indicates that its conversion to a perovskite under exposure to the MAI vapor is complete, and no unreacted PbI_2 remained in the films [38].

The spectroscopic ellipsometry study was performed for angles of incidence of 60° and 67° on a rotating analyzer ellipsometer equipped with an autoretarder (J. A. Woollam, Co. Inc.) for photon energies varying from 1.2 to 6.55 eV. To minimize possible degradation of the perovskite films under ultraviolet irradiation, the chosen instrument monochromatized the light before the mounted sample. To prevent the effect of moisture on the material properties, a dry atmosphere was maintained during the optical experiments. Furthermore, samples were stored in vacuum before measurements and all delay times were kept as short as possible.

The ellipsometric angles Ψ and Δ were recorded. A multilayer fit, including the sapphire substrate, the perovskite layer under study, and the surface roughness in the Bruggeman effective medium approximation, was performed. From this multilayer fit, the dielectric function of the perovskite layer was obtained via point-by-point fitting, i.e., no assumption on the line shape of the dielectric function was made. The resulting dielectric functions were successfully tested for the Kramers-Kronig consistency. The method yielded real and imaginary parts of the complex photon energy-dependent dielectric function with high accuracy.

III. RESULTS AND DISCUSSION

A. Crystal structure

There are three stable phases of the $CH_3NH_3PbI_3$ perovskite, e.g., a low-temperature orthorhombic phase, a tetragonal phase, which is stable at room temperature, and a cubic phase which is formed when $T > 330$ K [37,39]. Among these polytypes, when performing first-principles structural relaxations representing zero temperature, the low-temperature orthorhombic phase is favored. Since the goal of this work is to address the room-temperature experimental structures, and capture their optical properties, we retain the experimentally determined lattice constants for both the orthorhombic and cubic phases, while optimizing atomic coordinates using PBE to yield the minimum energy structures. We start with the experimental crystal structures taken from Ref. [40]: a $Pm\bar{3}m$ symmetry, 12-atom unit cell of the cubic phase with a lattice constant of $a = 6.391$ Å, and $I4/mcm$ symmetry, 48-atom unit cell of the tetragonal phase with lattice constants $a = 8.80$ Å and $c = 12.685$ Å. The full atomic relaxation results in the atomic structures of the unit cells of the cubic and tetragonal phases of $CH_3NH_3PbI_3$, as shown in Figs. 2(a) and 2(b), respectively. (The relaxed structures are available in the Supplemental Material [41].)

In our calculations the atomic relaxation leads to distortions, moving the Pb atom off the I-Pb-I center, thus breaking the inversion symmetry of the unit cell, which leads to Rashba splitting [42]. It was also suggested that this splitting could be controlled by an applied electric field. This could be crucial for photovoltaic applications, because Rashba splitting has been reported to reduce the recombination rate due to the presence of spin-forbidden transitions [43]. On the other hand, calculations based on DFT including van der Waals forces suggest that the extended carrier lifetimes in the $CH_3NH_3PbI_3$

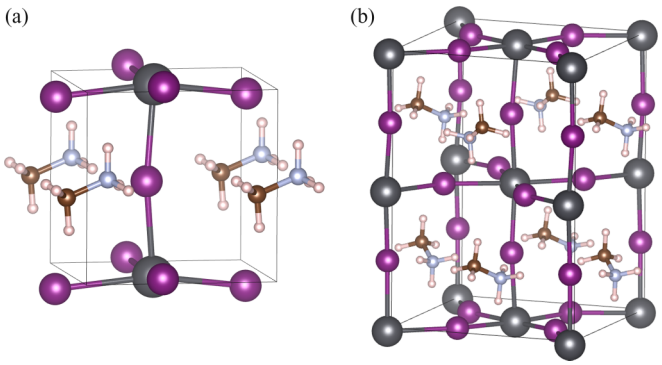

FIG. 2. Crystal structure of the unit cells of the (a) cubic phase and (b) tetragonal phase of $CH_3NH_3PbI_3$. Atoms are black (Pb), purple (I), brown (C), gray (N), and white (H).

perovskite could be due to dynamical changes of the band structure [44]. The motion of differently oriented CH_3NH_3 molecules leads to distortions of the perovskite octahedra, leading to a time-varying band structure with indirect band gaps, which suppresses electron-hole pair recombination.

Another complication arising from the structural features of $CH_3NH_3PbI_3$ is the effect of disorder due to the CH_3NH_3 groups rotating freely at room temperature [9]. The distortions due to rotating molecules contribute to Rashba splitting and lead to lower observed band gaps, compared to the ordered static case. This effect was recently addressed by the *GW* (with SOC) supercell calculations with randomized orientations of organic groups [18]. It was shown that although the band-edge states are mostly derived from the inorganic components with almost no hybridization with CH_3NH_3 groups, the organic molecules indirectly affect the band gap by introducing lattice relaxations and distortions to the inorganic cage.

Clearly, the structural properties and their influence on the electronic and optical properties of the $CH_3NH_3PbI_3$ perovskite present a number of complex problems. In this investigation, we address room-temperature optical properties of the $CH_3NH_3PbI_3$ perovskite. We find that using experimental lattice constants while allowing the atomic structures to relax in order to capture lattice distortions is adequate to address the band structure of $CH_3NH_3PbI_3$. The ellipsometry experiments performed here probe transitions related to the electronic band structure of the $CH_3NH_3PbI_3$ perovskite. Properties at lower frequencies, such as phonons, or contributions due to the rotational motion of $CH_3NH_3^+$ cations, are not accessed in our experiments, and therefore they are not addressed here.

B. Cubic phase: GGA electronic structure and optical properties

In order to describe the optical properties of the $CH_3NH_3PbI_3$ perovskite, we first calculate the basic GGA (PBE) band structure of the cubic phase, shown in Fig. 3, and compare the band structures computed with and without SOC.

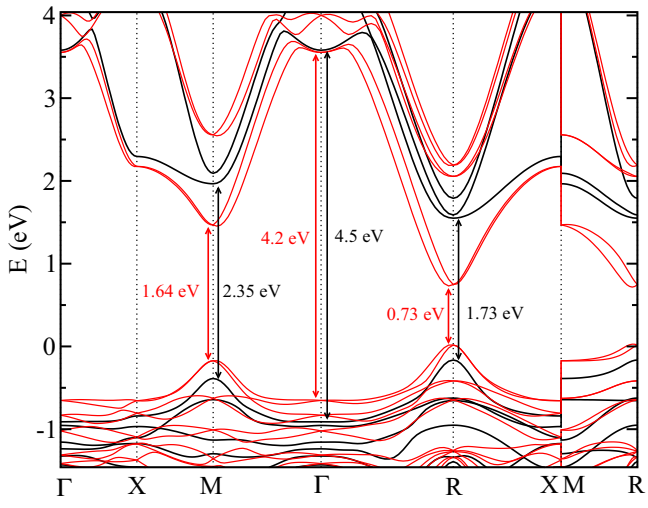

FIG. 3. GGA (PBE) band structure of the cubic phase of the $CH_3NH_3PbI_3$ perovskite, calculated with (red lines) and without (black lines) spin-orbit coupling. The path through the high symmetry points of the cubic lattice, $X = (0,1/2,0)$, $M = (1/2,1/2,0)$, and $R = (1/2,1/2,1/2)$.

Neglecting spin-orbit coupling, we obtain a direct band gap of 1.73 eV at the *R* point for the cubic phase, which is reasonably close to the experimentally measured gap of 1.6 eV. We note that theoretical GGA band-gap values reported in the literature vary between 1.2 and 1.7 eV. The spread in the reported values is likely due to differences in the crystal lattices, the orientations of the organic molecules, and the resulting atomic relaxations. The conduction band minimum at the *R* point is triply degenerate in the ideal cubic perovskite geometry [8]. In our calculations, the atomic relaxations lift this degeneracy by 0.24 eV. Similarly, at the *M* point, the twofold degeneracy is lifted as a result of atomic relaxations by 0.12 eV.

Including SOC in the GGA calculation significantly reduces the band gap by almost 1 eV, down to 0.73 eV, which is significantly lower than the experimental values. The drastic changes mostly originate in the Pb-derived conduction band states, where the value of the spin-orbit splitting is unusually large, i.e., 1.3 eV (often named a giant SOC), while the spin-orbit splitting of the iodine-derived valence band is also large, 0.42 eV. Thus, SOC further drives the bands apart that were initially split by the crystal fields due to atomic relaxations. As evident from a comparative analysis of the band structures computed with and without SOC, the valence and conduction band structure is significantly affected by SOC. Therefore, SOC should not be omitted in the calculations, even if doing so yields the correct band gap within GGA.

Recently, it was also suggested from the first-principles calculations that the alignment of methylammonium molecules alone does not significantly move the band-edge states. Instead, the relaxation of the atomic positions leads to an off-center displacement of the Pb atom, which induces a large Rashba splitting [45]. In our calculations this splitting in the conduction band minimum is found to be 18 meV, similar values at both the *R* and *M* points. Furthermore, it has been argued that since the PBE calculations that omit SOC yield the band gap in a reasonably good agreement with experiment, they should also accurately predict the optical properties of hybrid perovskites [13]. In order to evaluate the validity of this supposition, we calculate optical properties of the cubic $CH_3NH_3PbI_3$ perovskite within PBE-GGA, also testing the influence of the SOC. Figure 4 shows the PBE real and imaginary parts of the dielectric function calculated using the independent particle approximation with and without SOC, along with those derived from the ellipsometric data.

In the case when SOC is not taken into account, the GGA computed dielectric function is overestimated and nearly featureless. Even though the degeneracy in the conduction and valence bands is lifted by atomic relaxations, without SOC, the bands are sufficiently close to each other to produce a smooth absorption spectrum, and all optical transitions are averaged out by the integration over a dense *k*-point mesh. The experimentally measured curves, on the other hand, clearly show several peaks. Thus, the overall shape, structure, and values of the imaginary and real parts of the dielectric function are not well reproduced in non-SOC PBE calculations, in spite of the fact that in this case the band gap is closer to the experiment than in the SOC case. Inclusion of SOC introduces

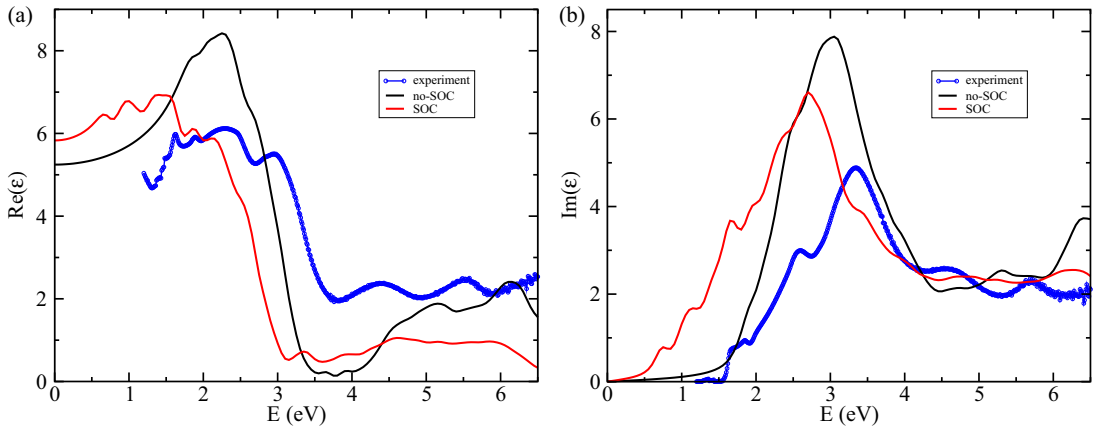

FIG. 4. Independent particle approximation GGA (PBE) calculated (a) real and (b) imaginary parts of the dielectric function of the cubic phase of the $CH_3NH_3PbI_3$ perovskite, with (red lines) and without (black lines) the spin-orbit coupling. The experimental ellipsometry measurement is shown with blue circles.

large spin-orbit energy splittings into the conduction and valence bands, as discussed above. This improves the overall structure of the calculated dielectric function and absorption, predicting the absorption peaks that are also observed in the experiment. However, the underestimated band gap shifts the spectra to lower energies by ∼1 eV, the energy error in the GGA calculated band gap. Nevertheless, since the band gap is significantly underestimated, the dielectric function and absorption spectrum are redshifted by approximately 1 eV in comparison with experiment. Therefore, a theoretical method which would better reproduce the experimental band structure is needed to describe the optical properties of the $CH_3NH_3PbI_3$ perovskite.

C. Cubic phase: HSE electronic structure and optical properties

Hybrid functionals have emerged in recent years as a new class of electronic structure methods, which significantly improved the agreement between calculations and experiment at an affordable increase in the computational cost. In a hybrid functional calculation, the local density (LDA or GGA) exchange-correlation part of the density functional is mixed with a Fock-type exchange part in varying proportions. In the HSE functional, the exchange-correlation interactions are separated into long- and short-range parts. The short-range part includes 25% of exact exchange and 75% of semilocal GGA exchange, while the long-range part is calculated with an approximate semilocal GGA expression [21]. The splitting is accomplished by introducing screening of the exact exchange interactions (similar to the screened exchange approach) with an optimal screening length of approximately 7–10 Å. HSE hybrid functionals significantly improve the band structure of most semiconductors [46]. In addition, effective masses are also improved, typically yielding values within a few percent of experiment [47]. However, in its standard form, with 0.25 fraction of exact exchange, the band gaps of most semiconductors still remain somewhat underestimated. For example, in the case of the $CH_3NH_3PbI_3$ perovskite, the HSE computed band gap at the R point (including SOC) is 1.15 eV. The spin-orbit splitting in the conduction band minimum (CBM), which is computed self-consistently, also increases to 1.45 eV, and the splitting in the valence band increases to 0.68 eV. In this case, the optical absorption and the frequency-dependent dielectric function (not shown here) are improved, however, there is still a notable shift to lower energies due to the underestimated band gap.

In light of the above, in order to recover the band structure that would agree with experimental measurements, we increase the ratio of exact exchange from 0.25 to 0.45, while keeping the exchange range separation parameter at 0.2. A similar parameter of 0.46 in HSE calculations of $CH_3NH_3SnBr_3$ and $CH_3NH_3SnI_3$ perovskites was also recently suggested [48]. Figure 5 shows the band structure of the $CH_3NH_3PbI_3$ perovskite calculated with the exchange-tuned HSE hybrid functional described above. The resulting band gap at the R point is now 1.57 eV, which is in very good agreement with experiments. The SOC in the conduction band is also increased to 1.54 eV, while that in the valence band is 0.87 eV. These

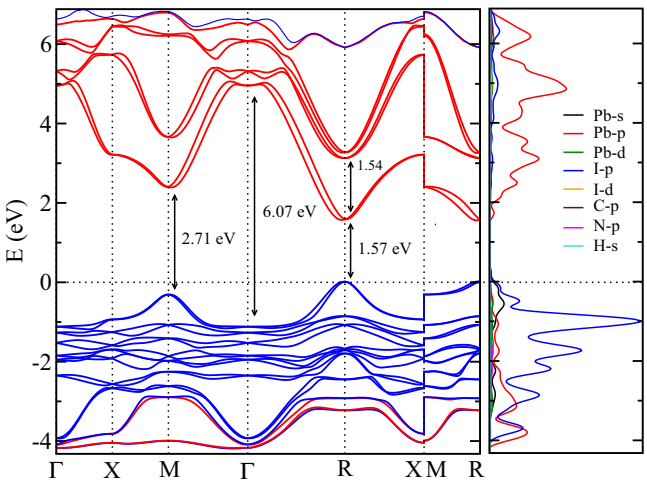

FIG. 5. Exchange-tuned HSE band structure of the cubic phase of the $CH_3NH_3PbI_3$ perovskite, including SOC. The right panel shows site- and l-projected densities of states on the same energy scale. Bands are color coded according to their predominant orbital character.

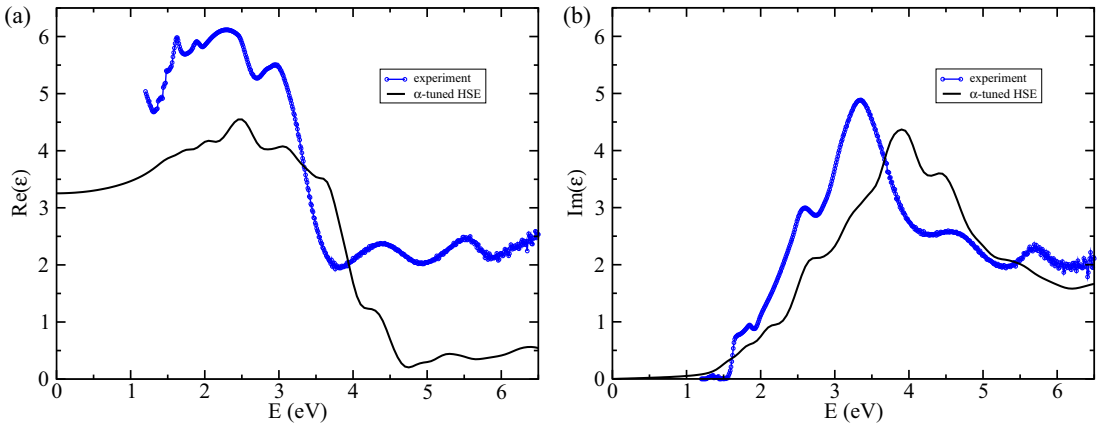

FIG. 6. (a) Real and (b) imaginary part of the dielectric function of the cubic phase of the $CH_3NH_3PbI_3$ perovskite calculated within the independent particle approximation using exchange-tuned HSE (including spin-orbit coupling). The experimental measurement is shown in blue circles.

values are larger than those obtained with standard HSE. The values of Rashba splitting at the conduction band minimum remain almost the same, 16 and 18 meV, at the *R* and *M* points, respectively.

In agreement with previous studies [15,18], we also find that the band structure around the band edges is mostly determined by the inorganic components of the hybrid perovskite. The valence band and conduction band extrema are derived from *p* orbitals of iodine and lead, respectively, as shown by the site- and *l*-projected densities of states (Fig. 5). There is almost no hybridization of the band-edge states with the states of the organic components. The organic molecules have an indirect effect on the band structure (but affecting mainly the crystal structure and its distortions); however, there is very weak coupling between the electronic states of the organic and inorganic components of the material.

It is important to note that it is possible to recover the experimental band gap by tuning the HSE functional without SOC. However, the important details of the band structure in the valence and conduction bands are lost in the process, i.e., without the large SOC driven splittings the structure of the experimental absorption spectrum and the frequency-dependent dielectric function cannot be reproduced. Thus, both the correct value of the band gap and the SOC are crucial to theoretically address the experiment. The exchange-tuned HSE hybrid functional with self-consistent SOC accomplishes this task.

Figure 6 shows the results of the exchange-tuned HSE calculation of the real and imaginary parts of the dielectric functions of the $CH_3NH_3PbI_3$ perovskite, within the framework of the independent particle approximation and including SOC. In spite of the fact that the band gap is tuned to match the experiment, the computed optical properties poorly compare to the experimentally obtained data. Overall, within the independent particle approximation, the HSE calculated real part of the dielectric function is underestimated when the correct band gap is recovered in this calculation. Tuning of the exact exchange exacerbates the problem, i.e., raising the Fock exchange ratio from 0.25 to 0.45 lowers the overall dielectric function curve by nearly a value of 1. However, a more important conclusion is that even though the computed band gap is correct, the calculated results are significantly blueshifted in comparison to experiment, due to the neglected electron-hole Coulomb interaction. For example, the measured peak of the absorption spectrum is about 0.5 eV lower in energy, even though the calculated absorption onset is in good agreement with the experiment. The overall conclusion is that optical spectra calculations that ignore excitonic effects yield unsatisfactory results, even when the band structure is recovered in the calculation.

D. Cubic phase: TD-HSE optical properties

Figure 7 shows the exchange-tuned TD-HSE computed dielectric function and optical absorption of the $CH_3NH_3PbI_3$ perovskite contrasted to the experimental ellipsometric measurements. The general features of the calculated excitonic peaks is significantly improved, although the dielectric function is still underestimated, as is the case for all HSE calculations performed here. However, the overall absolute values of the dielectric function are raised up to the level of the standard HSE, which is also an improvement over the independent particle picture. The absorption spectrum is also reproduced reasonably well with exchange-tuned TD-HSE. As expected, the overall spectra are redshifted compared to the independent particle calculation HSE. The exact exchange interaction range in the HSE functional ($\mu = 0.2$) appears appropriate for capturing weakly bound electron-hole pair interactions in the $CH_3NH_3PbI_3$ perovskite. TD-HSE calculations also predict four bound excitons below the fundamental HSE band gap with binding energies of 50–58 meV. However, there are a few calculated peaks that are not present in the experimental data. This discrepancy could be due to the averaging of random orientations of the methylammonia in the experimental samples, leading to statistical averaging of the local distortions and broadening of the individual absorption peaks.

E. Tetragonal phase: HSE electronic and TD-HSE optical properties

The band structure of the tetragonal phase is notably different from that of the cubic phase. The tetragonal phase

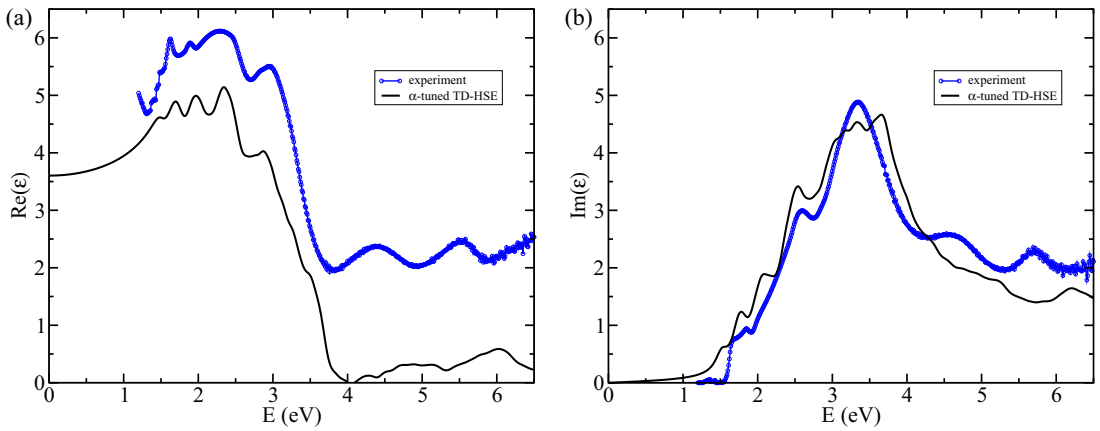

FIG. 7. Exchange-tuned TD-HSE calculated (a) real and (b) imaginary parts of the dielectric function of the cubic phase of the $CH_3NH_3PbI_3$ perovskite (including spin-orbit coupling). The experimental measurement is shown in blue circles.

is formed by rotating Pb - I_6 octahedra by ∼12° about the c axis in opposite directions in adjacent cubic cells along the c axis. This doubles the unit cell along the c axis, leading to the band folding in this direction. Most notably, this results in a merging of the R and Γ points of the cubic structure into the Γ point of the tetragonal structure. Therefore, as can be noted in Fig. 8, the band gap of the tetragonal phase is direct at the Γ point. Using the same fraction of exact exchange of 0.45, we obtain a band gap of 1.54 eV, which is slightly smaller than that of the cubic phase. As in the case of the cubic structure, the effect of SOC is also very significant. The SOC splittings below were evaluated by comparing Fig. 8 with the band structure of the tetragonal phase calculated without the SOC (not shown here). First, the calculated band gap is reduced by SOC by ∼1.1 eV (from 2.62 eV). Important changes are also introduced by SOC to the Pb p-orbital derived band that

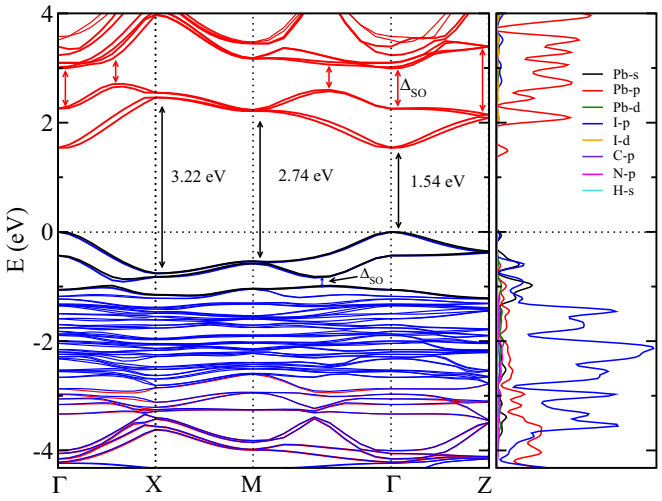

FIG. 8. Exchange-tuned HSE+SOC band structure of the tetragonal phase of the $CH_3NH_3PbI_3$ perovskite. The right panel shows site- and l-projected densities of states. Bands are color coded according to their orbital character. Red arrows indicate the SOC splitting in the conduction band. The path through the high symmetry points of the tetragonal lattice, $X = (0,1/2,0)$, $M = (1/2,1/2,0)$, and $Z = (0,0,1/2)$.

is about 1 eV above the conduction band bottom. This band is moved significantly upward, with degeneracies lifted by SOC, as shown by red arrows in Fig. 8. Here, each arrow shows the SOC splitting Δ_{SO} at the points where the bands would be degenerate in the absence of the SOC. At the Γ point, this splitting is 0.75 eV, which is roughly the value of the average SOC shift associated with this band. The iodine p-orbital derived valence band shows a significantly smaller SOC splitting of ∼0.16 eV, as also indicated in Fig. 8. Thus, the values of SOC splittings at the Γ point are similar in the cubic and tetragonal phases, in spite of the fact that the bands of the cubic R point are folded into the tetragonal Γ point, and the SOC splittings at the cubic R point are significantly larger, i.e., 1.54 and 0.87 eV in the conduction and valence bands, respectively.

The right panel of Fig. 8 shows the site- and l-projected densities of states, revealing the origin of the states around the band edge. In agreement with most previous findings, for example, most recently in Ref. [18], we find the valence band near the band edge to be derived mostly from iodine p orbitals with a small contribution from the lead p orbitals, similar to the cubic phase. The conduction band is formed almost entirely by the lead p orbitals. The contributions from the organic components to the states around the band edge are negligible. Several localized carbon and nitrogen orbitals derived from the corresponding p states are 6.5, 8.8, and 11.2 eV below the top of the valence band. Therefore, the measured absorption spectrum is affected by these organic molecules only indirectly via lattice distortions.

The calculated optical properties of the tetragonal phase of $MAPbI_3$ are similar to those of the cubic phase (Fig. 9). For example, in this case, TD-HSE calculations also find four bound excitons below the fundamental HSE band gap with binding energies of 45–51 meV. The overall structure of the absorption spectrum as well as the frequency-dependent dielectric function is in reasonable agreement with experiment. However, there are some notable differences compared to the case of the cubic phase (shown as a dotted line in Fig. 9). There are two calculated peaks around 3–3.5 eV in the absorption spectrum that are not present in the measured data. Although the room-temperature crystal structure of $CH_3NH_3PbI_3$ is tetragonal, the computed optical properties of the cubic phase

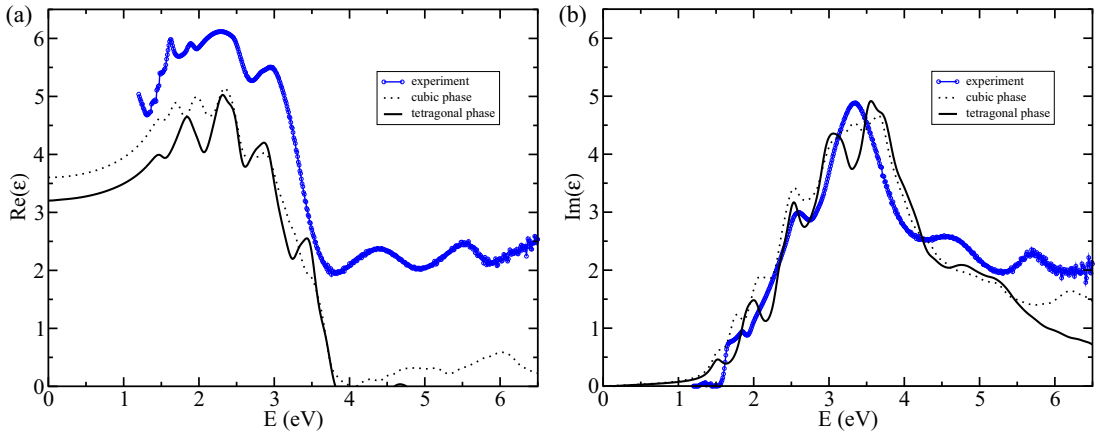

FIG. 9. Exchange-tuned TD-HSE calculated (a) real and (b) imaginary parts of the dielectric function of the tetragonal phase (solid line) of the $CH_3NH_3PbI_3$ perovskite (including spin-orbit coupling). The experimental measurement is shown in blue circles. The results for the cubic phase are shown as a dotted line for comparison.

appear to fit the experiment as well. The differences between the calculation and experimental conditions of the perovskite film could account for the discrepancies. The presence of disorder, interface strains, and the polycrystal nature of the samples would affect the experimentally measured absorption and dielectric function. Furthermore, at room temperature the organic molecules rotate, creating dynamical strains in the inorganic framework, which leads to a dynamical fluctuating band structure around the band edge. In a macroscopic sample, statistical averaging of these fluctuations would lead to a smoother absorption spectrum compared to the one calculated from an ordered static single crystal at zero temperature. Considering these differences between real experimental conditions and theory, the obtained agreement between calculations and measurements is satisfactory.

IV. CONCLUSIONS

We have performed a direct comparison of the optical properties of the $CH_3NH_3PbI_3$ perovskite obtained by several widely used theoretical methods with experiment. Specifically, through a comparative analysis of the calculated results with experimental ellipsometry measurements of the frequency-dependent real and imaginary parts of the dielectric function, we evaluate the applicability of the applied theoretical methods. Our results indicate that while the LDA/GGA without SOC can indeed lead to band gaps near the experimental values, some important details in the band structure away from the band edges are missing in both the valence and conduction bands. On the other hand, if the SOC is included in the LDA/GGA calculations, the resulting band gap is severely underestimated, as expected in local/semilocal approximations to the DFT. Importantly, we show that nonlocal hybrid functionals, such as HSE, can recover the correct band structure of the $CH_3NH_3PbI_3$ perovskite if the SOC is included in the calculations. Standard parametrization of the HSE with SOC reproduces the correct band structure, albeit with a slightly lower band gap. Tuning the HSE functional results in a band structure, which is in close agreement with experiment. However, HSE optical properties calculated within the independent particle approximation show notable differences as compared to experiments. Finally, time-dependent hybrid functional calculations (TD-HSE) of the optical properties, based on exchange-tuned HSE with SOC included in the calculation, produce absorption spectra and dielectric functions that are in good agreement with experiments.

ACKNOWLEDGMENT

The calculations were performed at the VCU Center for High Performance Computing.

[1] F. H. Alharbi and S. Kais, Renew. Sustain. Energy Rev. **43**, 1073 (2015)
[2] N.-G. Park, J. Phys. Chem. Lett. **4**, 2423 (2013).
[3] http://www.laserfocusworld.com/articles/2015/12/epfl-perovskite-solar-cells-reach-21-efficiency.html
[4] J. H. Heo, S. H. Im, J. H. Noh, T. N. Mandal, C. S. Lim, J. A. Chang, Y. H. Lee, H. J. Kim, A. Sarkar, M. K. Nazeeruddin, M. Gratzel, and S. I. Seok, Nat. Photon. **7**, 487 (2013).
[5] G. C. Xing, N. Mathews, S. Y. Sun, S. S. Lim, Y. M. Lam, M. Gratzel, S. Mhaisalkar, and T. C. Sum, Science **342**, 344 (2013).
[6] S. D. Stranks, G. E. Eperon, G. Grancini, C. Menelaou, M. J. P. Alcocer, T. Leijtens, L. M. Herz, A. Petrozza, and H. J. Snaith, Science **342**, 341 (2013).
[7] J. H. Noh, S. H. Im, J. H. Heo, T. N. Mandal, and S. I. Seok, Nano Lett. **13**, 1764 (2013).
[8] J. Even, L. Pedesseau, J.-M. Jancu, and C. Katan, J. Phys. Chem. Lett. **4**, 2999 (2013).
[9] J. Even, L. Pedesseau, and C. Katan, J. Phys. Chem. C **118**, 11566 (2014).
[10] G. Giorgi, J.-I. Fujisawa, H. Segawa, and K. Yamashita, J. Phys. Chem. Lett. **4**, 4213 (2013).

[11] E. Mosconi, A. Amat, M. K. Nazeeruddin, M. Grätzel, and F. De Angelis, J. Phys. Chem. C **117**, 13902 (2013).
[12] W.-J. Yin, T. Shi, and Y. Yan, Appl. Phys. Lett. **104**, 063903 (2014).
[13] M. Shirayama, H. Kadowaki, T. Miyadera, T. Sugita, M. Tamakoshi, M. Kato, T. Fujiseki, D. Murata, S. Hara, T. N. Murakami, S. Fujimoto, M. Chikamatsu, and H. Fujiwara, Phys. Rev. Appl. **5**, 014012 (2016).
[14] W.-J. Yin, J.-H. Yang, J. Kang, Y. Yan, and S.-H. Wei, J. Mater. Chem. A **3**, 8926 (2015).
[15] A. Filippetti and A. Mattoni, Phys. Rev. B **89**, 125203 (2014).
[16] P. Umari, E. Mosconi, and F. De Angelis, Sci. Rep. **4**, 4467 (2014).
[17] F. Brivio, K. T. Butler, A. Walsh, and M. van Schilfgaarde, Phys. Rev. B **89**, 155204 (2014).
[18] W. Gao, X. Gao, T. A. Abtew, Y.-Y. Sun, S. Zhang, and P. Zhang, Phys. Rev. B **93**, 085202 (2016).
[19] E. Menéndez-Proupin, P. Palacios, P. Wahnón, and J. C. Conesa, Phys. Rev. B **90**, 045207 (2014).
[20] W. Geng, L. Zhang, Y.-N. Zhang, W.-M. Lau, and L.-M. Liu, J. Phys. Chem. C **118**, 19565 (2014).
[21] J. Heyd, G. E. Scuseria, and M. Ernzerhof, J. Chem. Phys. **118**, 8207 (2003).
[22] J. Heyd, G. E. Scuseria, and M. Ernzerhof, J. Chem. Phys. **124**, 219906 (2006).
[23] Q. Chen, H. Zhou, Z. Hong, S. Luo, H.-S. Duan, H.-H. Wang, Y. Liu, G. Li, and Y. Yang, J. Am. Chem. Soc. **136**, 622 (2013).
[24] F. Hao, C. C. Stoumpos, Z. Liu, R. P. H. Chang, Q. Mercouri, and G. Kanatzidis, J. Am. Chem. Soc. **136**, 16411 (2014).
[25] S. Sharma, J. K. Dewhurst, A. Sanna, and E. K. U. Gross, Phys. Rev. Lett. **107**, 186401 (2011).
[26] M. Feneberg, M. F. Romero, M. Röppischer, C. Cobet, N. Esser, B. Neuschl, K. Thonke, M. Bickermann, and R. Goldhahn, Phys. Rev. B **87**, 235209 (2013).
[27] M. Landmann, E. Rauls, W. G. Schmidt, M. Röppischer, C. Cobet, N. Esser, T. Schupp, D. J. As, M. Feneberg, and R. Goldhahn, Phys. Rev. B **87**, 195210 (2013).
[28] J. P. Perdew, K. Burke, and M. Ernzerhof, Phys. Rev. Lett. **77**, 3865 (1996).
[29] P. E. Blöchl, Phys. Rev. B **50**, 17953 (1994).
[30] D. Hobbs, G. Kresse, and J. Hafner, Phys. Rev. B **62**, 11556 (2000).
[31] Implemented by G. Kresse and O. Lebacq, VASP manual, http://cms.mpi.univie.ac.at/vasp/vasp/vasp.html
[32] G. Kresse and J. Furthmuller, Phys. Rev. B **54**, 11169 (1996).
[33] M. Gajdoš, K. Hummer, G. Kresse, J. Furthmüller, and F. Bechstedt, Phys. Rev. B **73**, 045112 (2006).
[34] J. Paier, M. Marsman, and G. Kresse, Phys. Rev. B **78**, 121201 (2008).
[35] M. E. Casida, in *Recent Advances in Density Functional Methods*, edited by D. P. Chong (World Scientific, Singapore, 1995), Vol. 1.
[36] M. Methfessel and A. T. Paxton, Phys. Rev. B **40**, 3616 (1989).
[37] T. Baikie, Y. N. Fang, J. M. Kadro, M. Schreyer, F. X. Wei, S. G. Mhaisalkar, M. Graetzel, and T. J. White, J. Mater. Chem. A **1**, 5628 (2013).
[38] J. Burschka, N. Pellet, S.-J. Moon, R. Humphry-Baker, P. Gao, M. K. Nazeeruddin, and M. Grätzel, Nature (London) **499**, 316 (2013).
[39] N. Onoda-Yamamuro, T. Matsuo, and H. Suga, J. Phys. Chem. Solids **51**, 1383 (1990).
[40] T. Oku, in *Solar Cells—New Approaches and Reviews*, edited by L. A. Kosyachenko (InTech, Rijeka, Croatia, 2015).
[41] See Supplemental Material at http://link.aps.org/supplemental/10.1103/PhysRevB.94.075206 for atomic coordinates of relaxed structures of the cubic and tetragonal phases of $CH_3NH_3PbI_3$.
[42] M. Kepenekian, R. Robles, C. Katan, D. Sapori, L. Pedesseau, and J. Even, ACS Nano **9**, 11557 (2015).
[43] F. Zheng, L. Z. Tan, S. Liu, and A. M. Rappe, Nano Lett. **15**, 7794 (2015).
[44] C. Motta, F. El-Mellouhi, S. Kais, N. Tabet, F. Alharbi, and S. Sanvito, Nat. Commun. **6**, 7026 (2015).
[45] J. Li and P. M. Haney, in *2015 IEEE 42nd Photovoltaic Specialist Conference (PVSC)* (IEEE, New York, 2015), pp. 1–4.
[46] M. Marsman, J. Paier, A. Stroppa, and G. Kresse, J. Phys.: Condens. Matter **20**, 064201 (2008).
[47] Y.-S. Kim, M. Marsman, G. Kresse, F. Tran, and P. Blaha, Phys. Rev. B **82**, 205212 (2010).
[48] C. Bernal and K. Yang, J. Phys. Chem. C **118**, 24383 (2014).